



Analysis of Radio Frequency Blackout for the RAMC-II Flight Reentry Experiment

Alexandra Richet! Vivien Loridan? Luc Mieussens? Pierre Bonnemason! Thierry Magin⁵

Abstract

Under hypersonic regime conditions, a bow shock surrounds the spacecraft and temperature increases followed by electrons production that makes the gas behave like a weakly ionized plasma. This plasma layer reacts as a shield, either reflecting or capturing electromagnetic waves, leading to radio frequency blackout. The purpose of this work is to identify the most significant aerodynamic phenomena affecting electron density in the flow, and then to determine the resulting signal attenuation by solving electromagnetic equations through the connection between CFD (Computational Fluid Dynamics) and CEM (Computational Electromagnetics) inhouse codes.

In the current paper, the multi-species Navier–Stokes equations are employed in the aerodynamic simulations. Due to their low mass, electrons exhibit specific diffusion behavior that cannot be compared to other species and must be carefully modeled to accurately predict their transport around the vehicle. Special attention is given to the parameters and expressions governing diffusion fluxes by including an effective diffusion coefficient, which tends to reduce the electron density along the vehicle wall while increasing electron production at the stagnation front. In a subsequent phase, thermal nonequilibrium is taken into account by incorporating vibrational and electronic internal energy conservation equations into the Navier–Stokes system, each with dedicated source terms. This approach allows the flow to be characterized by multiple temperatures. CEM simulations are then performed to determine the signal attenuation at the telemetry's position over its specific frequency to predict RF blackout.

To validate the reliability of the coupled CFD–CEM model, simulation results are compared with the RAMC-II experimental data.

Keywords: aerodynamic, blackout, plasma layer, multi-species

Nomenclature

n – Species density

Latinp - Pressure q – Species charge c – Species mass fraction D – Diffusion coefficient q - Heat flux vector t – Time e – Internal energy E – Total energy T – Temperature f – Frequency \boldsymbol{v} - Velocity field E - Electric field GreekG – Signal gain ν - Frequency $\dot{\Omega}$ – Chemical source term h – Enthalpy J – Diffusive mass flux vector ρ – Density τ – Shear stress k_B – Boltzmann constant M – Molar weight Superscripts

C - Combination

HiSST-2025-01

 $^{^1}CEA-Cesta,\ 15\ avenue\ des\ Sabli\`eres-CS60001,\ 33116\ Le\ Barp\ Cedex,\ France,\ alexandra.richet@cea.fr$

²CEA-Cesta, 15 avenue des Sablières-CS60001, 33116 Le Barp Cedex, France, vivien.loridan@cea.fr

³IMB, 351 cours de la Libération-33400 Talence, France, luc.mieussens@u-bordeaux.fr

 $^{^4}$ CEA-Cesta, 15 avenue des Sablières-CS60001, 33116 Le Barp Cedex, France, pierre.bonnemason@cea.fr

⁵ VKI, 72 Chaussée de Waterloo, Rhode-Saint-Génèse, Belgique, thierry.magin@vki.ac.be

 $\begin{array}{cccc} D - Dissociation & i - Species \\ I - Ionization & m - Effective \\ Subscripts & p - Plasma \end{array}$

att – Attenuation tr – Translational-Rotational

c – Collisional v – Vibrational e – Electron/electronic

1. Contextualisation

During the reentry of Apollo 11, the vehicle traveled through various layers of the atmosphere at hypersonic speed. During this phase, Houston lost contact with the astronauts for at least four minutes. This communication cut-off resulted from the interaction between aerodynamic and electromagnetic phenomena, commonly referred to as blackout. This signal attenuation remains poorly understood by the community and is inadequately predicted by current theoretical models. The purpose of the present work is to improve the understanding of the aerodynamic phenomena that cause this electromagnetic shielding.

Under hypersonic reentry conditions, a bow shock surrounds the spacecraft, inside which the gases are compressed and slowed down. Most of the kinetic energy is converted into thermal energy, leading to a significant increase of temperature that triggers several physicochemical processes like dissociation, ionization and electronic excitation of molecules and atoms. These reactions tend to produce electrons within the flow around the vehicle, which behaves like a weakly ionized plasma. The plasma layer reacts as a shield, either reflecting or capturing electromagnetic waves emitted by relay satellite as represented in fig. 1.

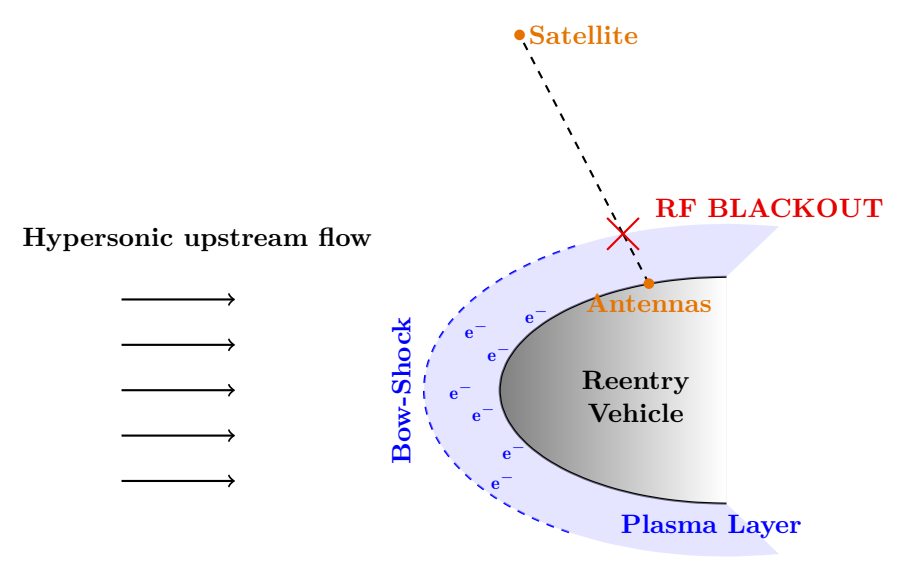


Fig 1. Scheme of RF Blackout during hypersonic reentry

Due to recurring radio blackouts during atmospheric reentry, the scientific community has devoted significant efforts to studying plasma behavior through both experimental and theoretical approaches. Following the Apollo missions, NASA conducted a serie of flight experiments in the late 1960s known as RAM (Radio Attenuation Measurement). The primary objective of these tests was to develop diagnostic techniques for characterizing reentry plasma parameters, such as electron density, and to assess potential in-flight mitigation strategies, including electrophilic injection. Instrumentation embedded onboard the vehicles recorded these parameters and documented communication losses across multiple frequency bands, as reported in NASA technical publications [1, 2]. The $RAM-C\ II$ flight in particular has become a widely referenced case in computational and theoretical studies related to RF blackout phenomena [1].

Later, in 1998, the European Space Agency (ESA) launched the Atmospheric Re-entry Demonstrator (ARD), which performed a suborbital flight reaching an altitude of approximately 830km. One of the main objectives of this mission was to investigate radio communication behavior during atmospheric reentry. During the descent phase, a complete RF blackout was observed at GPS frequencies, while strong attenuation of the TDRS signal occurred between altitudes of 86km and 44km [3]. Other reentry vehicles, such as OREX, IXV, Stardust, and ATV, have also experienced similar phenomena, further highlighting the need for accurate modeling and mitigation of RF blackout during hypersonic flight. To address this issue, it is necessary to better understand the complex physical phenomena underlying these communication cutoffs, originating from both aerodynamic and electromagnetic effects. The plasma layer that reflects or absorbs electromagnetic waves is primarily governed by electron density, which is predicted through Computational Fluid Dynamics (CFD) calculations. Historically, the flow was modeled as a gas in thermochemical equilibrium. However, under reentry conditions, taking account for chemical nonequilibrium is strongly recommended to accurately capture the behavior of electrons, ionized species, and neutrals. The flow is therefore described using a multi-species model, as presented by [4]. This chemical nonequilibrium has a direct impact on the prediction of electron density as developed in [5]. Later, the role of thermal nonequilibrium was emphasized, influencing the final electron density through the consideration of a distinct electronic temperature, as proposed in [4, 6–8]. These works focused on the impact of these nonequilibrium assumptions on flow parameters and highlighted significant variations in the evolution of electron density depending on the model used. As a result, aerodynamic outputs are commonly transferred to electromagnetic solvers to assess the influence of the plasma layer on electromagnetic wave attenuation and to predict RF blackout. Takahashi et al. [9] validated a coupled CFD–CEM model called FD2TD (Finite-Difference Time-Domain method) for the ARD mission. The ICARE vehicle has also been developed to mitigate communication loss by employing an inflatable reentry design aimed at altering flow characteristics around the vehicle [10].

The purpose of this work is to improve the physical models within the in-house aerothermal code to accurately describe electron density under reentry conditions, thereby enabling reliable prediction of RF blackout. This is achieved by coupling CFD results with an in-house electromagnetic solver to analyze signal attenuation. To address this objective, the present paper is organized as follows. First, the multi-species model is described, highlighting the influence of diffusion processes and chemical reaction schemes, followed by an analysis of the impact of a multi-temperature approach. Secondly, the electromagnetic parameters and solvers used to compute signal attenuation at the antenna locations are briefly presented. Finally, the entire computational chain is validated by comparing the results with experimental data from the $RAM-C\ II$ flight experiment.

2. Aerodynamic Model

Simulations of the surrounding flow during reentry were carried out using CFD codes based on the Navier–Stokes equations, in order to reliably model the physical phenomena involved. In such conditions, thermochemical nonequilibrium arises and affects temperature and electron density that govern the properties of the surrounding gas. Chemical nonequilibrium occurs when the timescale of chemical reactions is comparable to that of transport/advection. The nonequilibrium Navier-Stokes equations are based on multi-species models. Adding chemical source terms in the system of equations introduce the chemical nonequilibrium behavior caused by the reentry conditions and describes mass variation of each species. The aerodynamic code used in this study solves Navier-Stokes equations by considering a fluid composed of neutral and ionized species.

2.1. Navier-Stokes Solver

The CFD code currently developed at CEA-CESTA solves the 2D axisymmetric and 3D Navier–Stokes equations. Currently, chemical nonequilibrium is assumed (multi-species reacting flow). The conservation equations can be expressed under a conservative form:

$$\frac{\partial \boldsymbol{U}}{\partial t} + \boldsymbol{\nabla} \cdot \underline{\underline{F}} = \boldsymbol{S}, \quad \boldsymbol{U} = \begin{pmatrix} \rho_i \\ \rho \boldsymbol{v} \\ \rho E \end{pmatrix}, \quad \boldsymbol{S} = \begin{pmatrix} \dot{\omega}_i \\ 0 \\ 0 \end{pmatrix}$$
(1)

where v is the velocity field, E the total energy, \mathbf{U} is the vector of conserved variables and \mathbf{S} the vector of source terms. The previous vectors are expressed for each species i, with ρ_i representing the species density and $\dot{\omega}_i$ the source term that governs the production or consumption of species i through chemical reactions.

The flux tensor presented in (1) is $\underline{\underline{F}} = \underline{\underline{F}_c} - \underline{\underline{F}_v}$ where is F_c the inviscid flux and F_v is the viscous flux rescreetively given by:

$$m{F_c} = egin{pmatrix}
ho_i m{v} \
ho m{v} \otimes m{v} + p m{I} \
ho H m{v} \end{pmatrix}, \quad m{F_v} = egin{pmatrix} - m{J}_i \ au \ - m{q} + au m{v} \end{pmatrix}$$

with p the pressure, τ the shear stress tensor and H the total ethalpy. Mass fluxes are described in the following section. The viscous stress tensor is related to a Newtonian fluid by

$$\tau = \mu \left[(\boldsymbol{\nabla} \otimes \boldsymbol{v}) + (\boldsymbol{\nabla} \otimes \boldsymbol{v})^{\top} \right] + \lambda (\boldsymbol{\nabla} \cdot \boldsymbol{v}) \mathbf{I}$$

with $\lambda = -\frac{2}{3}\mu$ according to Stokes' hypothesis. The mixture viscosity μ is obtained via Wilke's semi-empirical rule [11], with species viscosities calculated using Blottner's model [12]. Heat fluxes involved in the energy conservation equation are modeled as:

$$\mathbf{q} = -\kappa \nabla T + \sum_{i} h_{i} \mathbf{J}_{i},$$

including contributions from thermal conduction and diffusion, where κ is the mixture thermal conductivity calculated using the Prandtl number as $\kappa = \frac{\mu C_p}{P_r}$, with $P_r = 0.67$, with C_p the specific heat at constant pressure. The solver computes physical quantities such as the density ρ , species mass fractions c_i , velocity components u and v, temperature T, and pressure p from the conservative variables. The total gas density is obtained as $\rho = \sum_i \rho_i$, which allows the determination of the velocity components u and v, as well as the species mass fractions c_i , calculated by $c_i = \frac{\rho_i}{\rho}$. The gas temperature is found by solving for the internal energy e through an iterative Newton method, using the relation $E - \frac{1}{2}(\mathbf{v} \cdot \mathbf{v}) = e(T)$. Finally, the pressure is calculated by assuming each species behaves as a perfect gas and applying Dalton's law of partial pressures, yielding $p = \sum_i p_i = \sum_i \frac{\rho_i RT}{M_i}$. Numerically, the code solves the Navier-Stokes equations using multi-block structured grids, employing a finite-volume formulation for inviscid fluxes and a finite-difference approach for viscous fluxes. The solution of this system of equations is advanced towards a steady state through a time implicit scheme, which requires the calculation of the Jacobian matrices associated with the inviscid and viscous flux tensors, as well as the source terms.

2.2. Diffusion model

Due to the production on ionized species, the flow is affected by an electric field that influences the diffusion of ionized species and subsequently of other species. Because of their low mass, electrons behave distinctly from heavier species, necessitating the use of refined, electron-focused models to accurately capture plasma evolution. Modeling ionized fluids requires precise treatment of species diffusion, while ensuring mass and current conservation throughout the entire domain. The most basic strategy consists in modeling mass fluxes according to Fick's law.

$$\mathbf{J}_i = -\rho D_i \nabla \mathbf{c}_i$$

where c_i is the mass fraction and D_i the diffusion coefficient of species i. The diffusivity model for each species is, as a first approximation, given by the Lewis model $\rho D = \frac{\kappa L_e}{C_p}$, where L_e is the Lewis number, set to 1.4. However, due to the low mass of electrons, this model does not accurately capture their transport through the fluid, particularly within the plasma layer. This motivates improving the model by assigning a distinct diffusion coefficient to each species while ensuring conservation of total mass $(\sum_i \mathbf{J_i} = \mathbf{0})$ and electric current $(\sum_i q_i \mathbf{J_i} = \mathbf{0}, q_i)$ being the charge per unit of mass of the species i) within the flow domain. In Blotnner's work [12], a mass conservation model is suggested as follows:

$$\mathbf{J_i} = \mathbf{J_i^*} - c_i \sum_{j} \mathbf{J_j^*} \quad \text{with} \quad \mathbf{J_i^*} = -\rho D_{im} \nabla \mathbf{c_i}$$
 (2)

where the first expression is the correction formulation, J_i^* is the uncorrected diffusional mass fluxes and D_{im} the effective diffusion coefficient of species i. In this work, effective diffusion coefficients are calculated according to [13] expression:

$$D_{im} = \frac{1 - x_i}{\sum_{i \neq j} \frac{x_j}{B_{ij}}} \tag{3}$$

where B_{ij} is the binary diffusion coefficient associated to collision integrals. In this current study, the effective diffusion coefficients are calculated using the Mutation++ library [14]. As it is presented, this expression ensures the conservation of mass. However, under reentry conditions, the surrounding flow becomes weakly ionized due to the rapid increase in temperature, which leads to the production of ionic species and electrons. The electric field must be taken into account because it influences the diffusion of charged species; therefore, the electric current must be conserved.

The work of [15] and [16] developed mass fluxes correction based on a model for ambipolar diffusion in plasmas known as the Self-Consistent Effective Binary Diffusion (SCEBD) approximation. In a mass fraction formulation, the uncorrected diffusional mass fluxes can be written as:

$$\mathbf{J}_{\mathbf{i}}^* = -\rho D_{im} \nabla \mathbf{c}_{\mathbf{i}} + \rho M_i \rho_i D_{im} q_i \mathbf{E}$$
(4)

with **E** denoting the electric field. To ensure the conservation of the fluid current (i.e. $\sum_i q_i \mathbf{J}_i = 0$), the electric field is expressed as $\mathbf{E} = \frac{\sum_i M_i q_i D_{im} \nabla \mathbf{c}_i}{\sum_i M_i q_i^2 \rho_i D_{im}}$. This expression is derived under the assumption that the flow is electrically neutral $(\sum_i c_i q_i = 0)$.

However, as mentionned in [16], during convergence, local charge was formed, which enables simulation to converge. To address this issue, the local charge term must be retained in the mass flux diffusion equation to ensure the convergence of the calculations. The assumption of electric neutrality is achieved and validated upon simulation convergence. Under such circumstances, the uncorrected diffusional mass fluxes can be expressed as:

$$\mathbf{J}_{\mathbf{i}}^{*} = -\rho D_{im} \nabla \mathbf{c}_{\mathbf{i}} + \rho M_{i} D_{im} \left[\rho_{i} q_{i} - c_{i} \sum_{k} \rho_{k} q_{k} \right] \mathbf{E}$$
(5)

2.3. Thermal Nonequilibrium

During reentry, the vehicle travels through different layers of the atmosphere, which trigger various types of thermodynamic nonequilibrium. At high altitudes, thermal nonequilibrium has to be considered, and the different internal energy modes become decoupled. The fluid under study can then be characterized by multiple temperatures, each associated with a specific internal energy mode. The different energy modes can be sorted into four main groups: translational (motion of the entire molecule through space), rotational (rotation of the atoms about the molecule's center of mass), vibrational (oscillatory motion of atoms relative to the molecular barycenter), and electronic (transitions of electrons between different energy levels). Different assumptions can be made regarding the influence of each internal energy mode, and some of them can be directly coupled. Most of the time, the translational and rotational modes are grouped together, as their associated temperatures are generally assumed to be equal. In a two-temperature model, the translational and rotational modes are combined and assigned a common temperature, while the vibrational and electronic modes are grouped and associated with a second temperature. In the current paper, a three-temperature model is considered, for which the vibrational and electronic modes are treated separately, each with its own temperature, allowing for a more detailed description of thermodynamic nonequilibrium. In such case, two internal energy equations are added to the Navier-Stokes system: one for vibrational energy and one for electronic energy. These equations are directly associated with source terms that arise from the interaction between internal energy modes (e.g., VE for Vibrational–Electronic, VT for Vibrational–Translational) or from chemical reactions (e.g., I for ionization, D for dissociation) [17]. The complementary equations are:

$$\frac{\partial \rho e_v}{\partial t} + \nabla \cdot (\rho e_v v) - \nabla \cdot (\kappa_v \nabla T_v) - \nabla \cdot \left(\rho \sum_{s=m} \epsilon_{vs} D_s \nabla c_s\right) = \dot{\Omega}_v$$
 (6)

for vibrational internal energy, where $\dot{\Omega}_v = \dot{\Omega}^{VT} + \dot{\Omega}^{VE} + \dot{\Omega}_v^D$, and

$$\frac{\partial \rho e_e}{\partial t} + \nabla \cdot (\rho e_e \mathbf{v}) + p_e \nabla \cdot \mathbf{v} - \nabla \cdot (\kappa_e \nabla T_e) - \nabla \cdot (\rho h_e D_e \nabla c_e) = \dot{\Omega}_e$$
 (7)

for electron-electronic internal energy, where $\dot{\Omega}_e = \dot{\Omega}^{ET} - \dot{\Omega}^{VE} + \dot{\Omega}_e^D + \dot{\Omega}_e^I + \dot{\Omega}_e^C$.

3. Electromagnetic Solver

The electromagnetic code used in this study enables to calculate the signal attenuation at the position of the telemetry system or antenna on the reentry body. All relevant physical models and numerical methods used in the solver are described in this section.

3.1. Radio-Communication theory

Due to the abrupt increase in temperature during reentry, chemical reactions are triggered—most notably ionization—which rapidly generates a large number of free electrons around the spacecraft. As a result, the surrounding fluid becomes weakly ionized, leading to the formation of a plasma layer that surrounds the vehicle. This plasma layer is characterized by a specific parameter known as the plasma frequency, which serves as a critical threshold. When the frequency of the incoming radio wave is lower than this plasma frequency, the wave is totally reflected, preventing signal transmission. The plasma frequency [18] is formulated as:

$$f_p = \frac{1}{2\pi} \sqrt{\frac{e^2 n_e}{\varepsilon_0 m_e}} \tag{8}$$

where n_e , e, m_e and ε_0 are respectively the electron density, the elementary charge $(1.602 \times 10^{-19} \text{ C})$, the electron mass $(9.11 \times 10^{-31} \text{ kg})$ and the permittivity in free space $(8.854 \times 10^{-12} F.m^{-1})$. The role and influence of free electrons are important in the investigation of RF blackout, as they directly affect radio signals propagation. In this context, the plasma layer behaves as an electromagnetic shield. Radio signals emitted by a relay satellite or a ground station along the line of sight are either reflected by the plasma sheath or trapped within it, leading to a disruption in communication. Moreover, to characterize a plasma, the electron collision frequency [17] is the average number of collisions an electron undergoes per unit time with other particles. It determines how easily electrons respond to electromagnetic fields—high collision frequency reduces their mobility and energy absorption, while low collision frequency allows stronger interaction with the field. The collision frequency is expressed as:

$$\nu_c = \sum_i n_i v_e \pi \Omega_{e-i}^{1,1} \tag{9}$$

where $v_e = \sqrt{\frac{8k_BT}{\pi m_e}}$ is the average thermal velocity of the electrons and $\pi\Omega_{e-i}^{1,1}$ is the collision integral between electrons and heavy species [19]. These two parameters enable to compute the plasma electric permittivity, which is the key quantity to characterize the wave propagation in the ionized flow (i.e. $\varepsilon_r = 1 - \frac{f_p^2}{f_{link}\left(1-j\frac{\nu_c}{f_{link}}\right)}$ with f_{link} the emitted communication frequency).

3.2. Inhouse electromagnetic code

The inhouse electromagnetic code is developped at CEA. It solves the Maxwell's equations in a harmonic regime [20]. Maxwell's equations are expressed by the following system:

$$\begin{cases}
\nabla \cdot \vec{E} = \frac{\rho_c}{\varepsilon_0} \\
\nabla \cdot \vec{B} = 0 \\
\nabla \times \vec{E} = -\frac{\partial \vec{B}}{\partial t} \\
\nabla \times \vec{B} = \mu_0 \vec{J} + \mu_0 \varepsilon_0 \frac{\partial \vec{E}}{\partial t}
\end{cases}$$
(10)

where \vec{E} , \vec{B} and \vec{J} are respectively the electric, magnetic and current field vectors and ρ_c is the charge

The code solves Maxwell's equations in the frequency domain for a 2D axisymmetric geometry, discretized using an unstructured triangular mesh. The equations are formulated using either surface or volume finite element methods, depending on the physical quantity involved. It is important to note that the code assumes the studied vehicle acts solely as a receiver of electromagnetic waves. The solver computes the resulting electromagnetic field based on the properties of the surrounding fluid and the frequency of the incident wave. To evaluate the influence of the plasma layer on the electromagnetic field, it is possible to determine the attenuation of the emitted signal by comparing the electric field with and without the presence of plasma. The signal attenuation is based on [21] and defined as:

$$G_{att} = -20\log_{10}(\frac{|\mathbf{E}_{\mathbf{plasma}}|}{|\mathbf{E}_{\mathbf{free}}|}) \tag{11}$$

where $|E_{plasma}|$ and $|E_{free}|$ are respectively the electric field with and without plasma. The last term of eq. (11) represents the wave reflected backwards to the emitting source. To evaluate the signal attenuation, the electric field amplitudes for both transverse electric (TE) and transverse magnetic (TM) polarizations are computed at a specific location, corresponding in this study to the position of the RAM-C antenna. Two simulations are performed in parallel: one considering air as the only fluid, and another incorporating plasma effects. From these components, a range of electric field is then defined as:

$$\mathbf{E} = [min(\mathbf{E}_{TM}, \mathbf{E}_{TE}); max(\mathbf{E}_{TM}, \mathbf{E}_{TE})] \tag{12}$$

Once this calculation is performed for both simulations, the signal attenuation can be determined using equation (11). According to NASA, if the signal attenuation exceeds 30 dB, the vehicle experiences a "Radio Frequency Blackout" [22]. The identification of blackout in this study is based on this criterion.

4. Validation of the improved aerodynamic model

4.1. Presentation of the RAM C-II experiment and freestream conditions

Due to the recurring radio blackout during reentry, the scientific community focused on studying the plasma behavior both experimentally and theoretically. RAM-CII serves as a reference case for numerous computational and theoretical studies on RF blackout. In this experiment, the goal was to determine the electron density that characterizes the plasma sheath in hypersonic regime from data collected by embedded radio reflectometers and electrostatic probes. The RAM C-II is a 9 deg sphere-cone with a 30.48 cm nose diameter berrylium cap and a total length of 129.54 cm teflon body (cf. fig. 2). The current numerical study refers to the following trajectory point quoted in table 1.

Altitude [km]	Mach number	Velocity $[m.s^{-1}]$	Density $[kg.m^{-3}]$
71	25.9	7651	7.644×10^{-5}
61	23.9	7651	2.703×10^{-4}
51	18	7620	9.069×10^{-4}

Table 1. RAM C-II Freestream conditions

Additionally, the boundary conditions include a wall temperature of 1200 K and a Neumann condition at the wall, expressed as: $\frac{\partial c_i}{\partial \mathbf{n}} = 0$

Moreover, in all subsequent results, the flow is assumed to be in chemical nonequilibrium. It consists of 11 chemical species: N_2 , O_2 , NO, N, O, NO^+ , e^- , O^+ , N^+ , N_2^+ , O_2^+ governed by a reaction mechanism involving 49 chemical reactions [19, 23, 24].

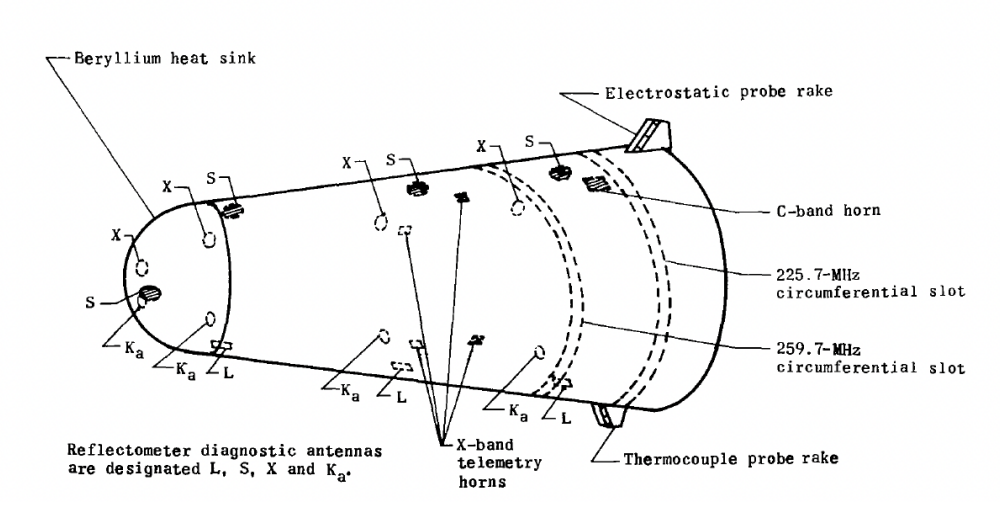


Fig 2. RAMC-II Scheme with antenna locations from [1]

4.2. Improvement of the electron density prediction

Currently, the RF blackout is not accurately predicted and so on models have to be improved to deal with the current challenges. Aerodynamic simulations were conducted at the three enunciated altitudes (cf. table 1), but they resulted in incorrect signal attenuation estimations (cf. table 2). However, as

Altitude [km]	71	61	51
$G_{att,VHF}$ [dB]	19.9 - 22.6	27.8 - 39.4	14.1 - 14.8
$G_{att,C-Band}$ [dB]	0.0	0.0	0.0 - 0.3

Table 2. VHF (225,7MHz) and C-Band (5.8GHz) Signal Attenuations of the RAM C-II during reentry with Lewis diffusion model

previously explained, RF blackout is considered to occur when the signal attenuation exceeds 30 dB. For the RAM C-II vehicle, VHF blackout was recorded from altitudes 76 km to 23 km and for the C-Band from altitudes 51km to 38 km [25]. From the first computation with Lewis diffusion model, no blackout is detected at 51 km for both studied communication frequencies, indicating that the plasma layer is not correctly modeled, particularly the electron density.

As a consequence, more accurate models governing electron density must be developed in order to reliably predict communication interruptions, and a preliminary study is presented in the following sections.

4.2.1. Improved diffusion model

As previously discussed, the current simulation leads to an overestimation of the electron density. One possible explanation for this issue may lie in the treatment of Lewis diffusion, which is not accurate to deal with electron transport. When the effective diffusion coefficient is used, mass conservation within the fluid is no longer guaranteed. Additionally, due to the consideration of chemical nonequilibrium, chemical reactions occur, leading to the weakly ionized behavior of the fluid. As a result, electric current is also not conserved. Consequently, it becomes necessary to compute correction terms for both mass and electric current within the diffusive mass flux vector (cf. 2 and 5). In fig. 3, the electron density in the flow field is presented at various altitudes. For each case, the top and bottom maps respectively show n_e obtained using Lewis and effective diffusion coefficients. The electron distribution varies significantly between the two models. When effective diffusion coefficients are employed, the plasma sheath extends more broadly along the vehicle surface and into the spacecraft's wake. Consequently, the electron density peak at the vehicle's front becomes significantly higher, for instance, at 61 km, $n_e = 2.69 \times 10^{20} \,\mathrm{m}^{-3}$ in the Lewis

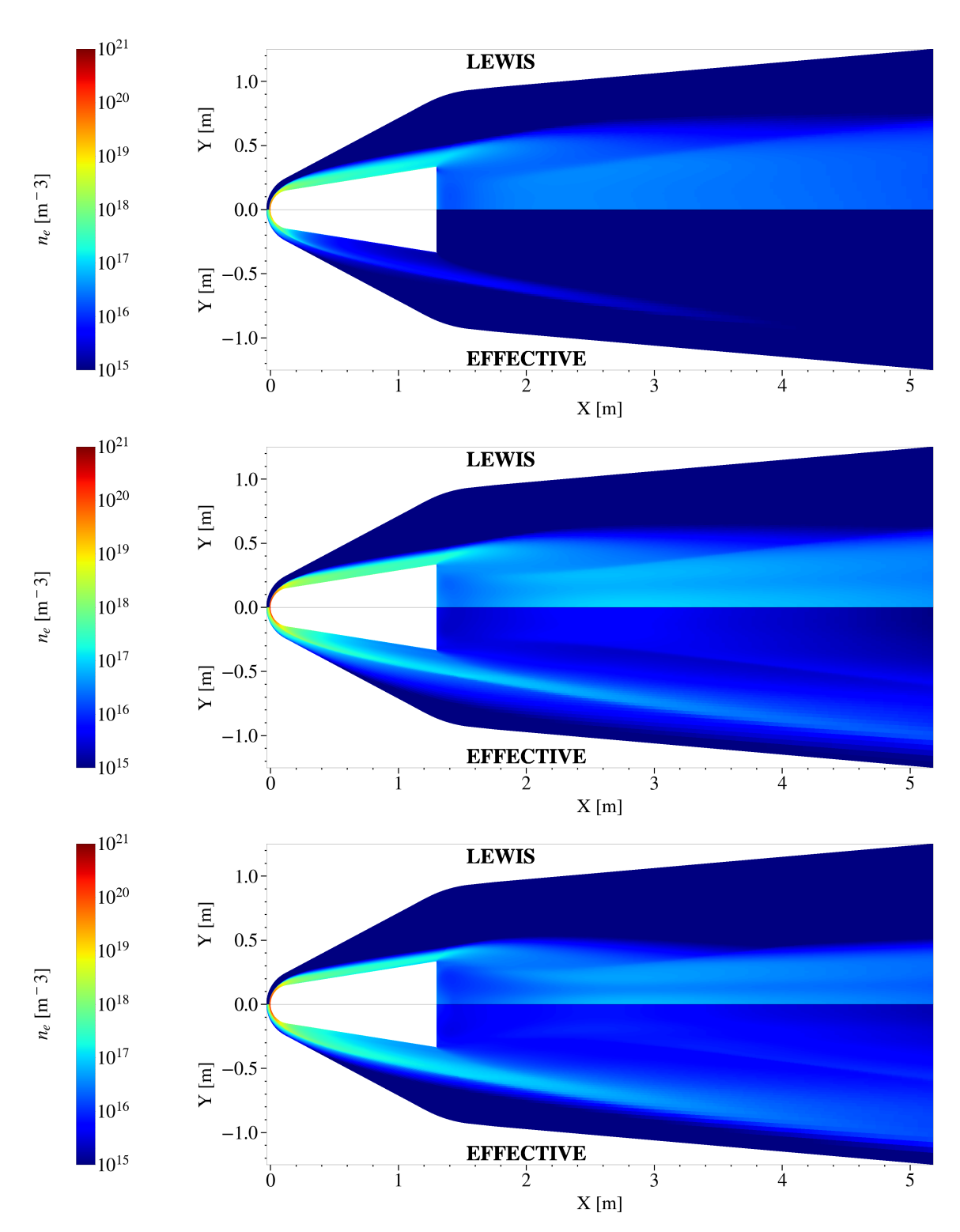


Fig 3. Comparaison of diffusion coefficients models with maps of n_e at altitudes 71km (top), 61km (middle) and 51km (bottom)

case compared to $n_e = 8.171 \times 10^{20} \,\mathrm{m}^{-3}$ with effective coefficients. Moreover, electrons are transported upstream, ahead of the bow shock, unlike in the Lewis model, where they remain confined near the shock

layer. Along the wall, electron density tends to decrease in simulations using effective diffusion, whereas it remains more uniform in the Lewis model across all altitudes. A final observation from these figures is that, in the Lewis model, the highest electron density occurs at 61 km, whereas in the effective diffusion model, it occurs at 51 km. According to experimental data, the electron density should indeed peak at 51 km, as all telemetry signals were saturated and both VHF and C-band communications experienced a complete blackout at that altitude. A closer view of the electron density along the stagnation line is

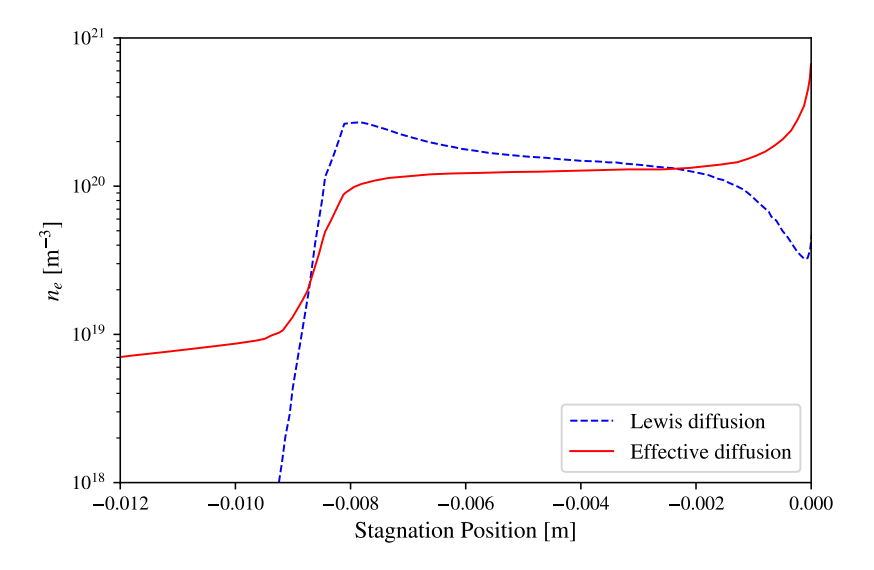


Fig 4. Comparaison of diffusion coefficient models at 61 km on stagnation line

shown in fig. 4. In the Lewis model, electrons are produced at the bow-shock tend to stabilize between the bow shock and the vehicle nose. In contrast, with effective diffusion coefficients, electron production is concentrated near the vehicle wall and are diffused in front of the bow-shock too. This indicates that the region close to the surface becomes particularly rich in ionized particles and free electrons. To assess

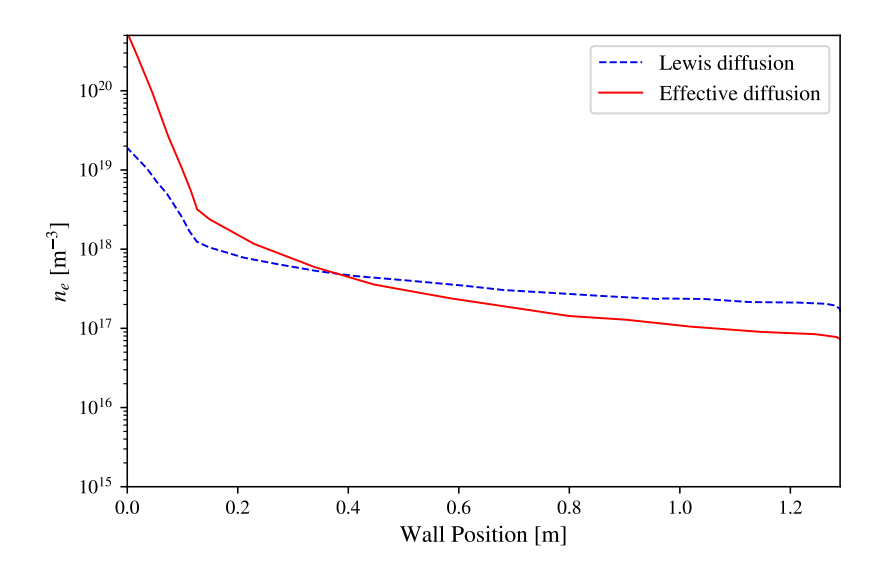


Fig 5. Comparaison of n_e in function of the diffusion model at 51km

the reliability of the models, a comparison is made between the computed electron density along the

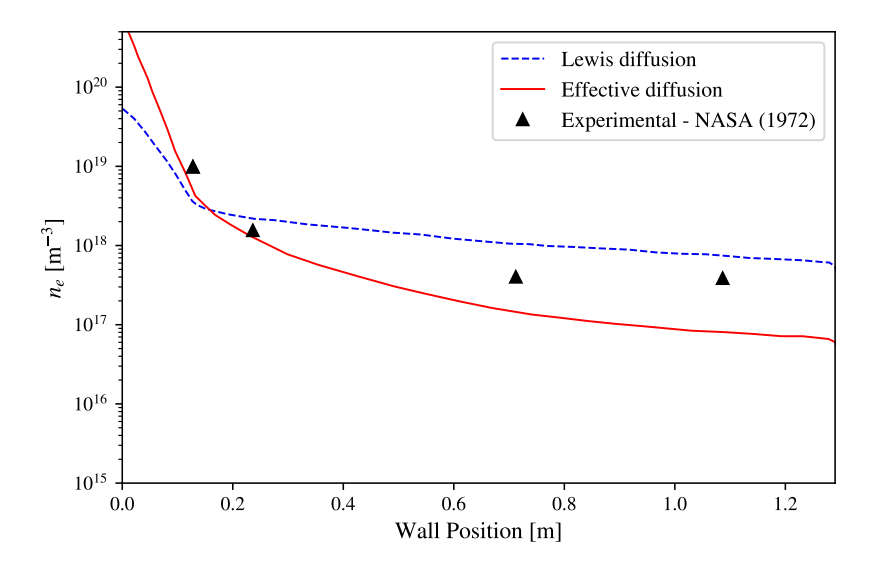


Fig 6. Comparaison of n_e in function of the diffusion model at 61km with experimental data

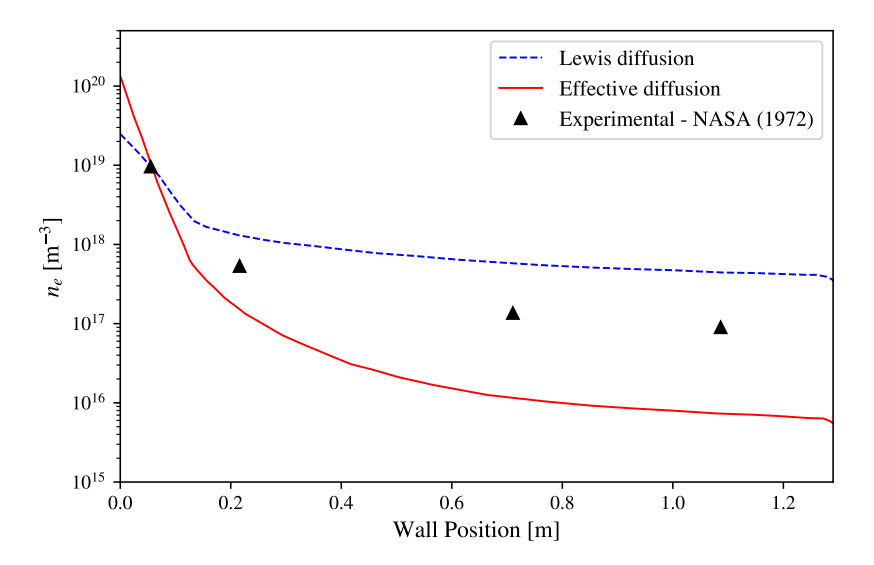


Fig 7. Comparaison of n_e in function of the diffusion model at 71km with experimental data

vehicle wall and the experimental data provided by NASA [1]. In fig. 7, fig. 6 and fig. 5, this comparison is presented for three different altitudes: 71km, 61km and 51km. At 51km, the electron density around the vehicle nose is higher in the effective diffusion model than in the Lewis diffusion model. However, along the vehicle wall, the predicted electron densities are similar for both diffusion models. At 61km, the electron density computed using effective diffusion coefficients provides a more accurate prediction at the front of the vehicle compared to the Lewis model. But, along the wall, the Lewis model tends to overestimate the electron density, while the effective diffusion model tends to underestimate it. At 71km, the effective model further increases the discrepancy between the numerical and experimental results. In fact, the higher the altitude, the greater the divergence in electron density predictions is near the vehicle wake between the two diffusion models. The simulations reveal that the effective model underestimates the electron density at the locations of the VHF and C-band antennas (see fig. 2).

4.2.2. Influence of multi-tempratures model

During reentry, the vehicle passes through different layers of the atmosphere. At high altitudes, thermal nonequilibrium is triggered. The flow can then be characterized by multiple temperatures, each associated with a specific internal energy mode namely electronic, rotational, translational, and vibrational. First, a study on the importance of thermal nonequilibrium is carried out as a preliminary step before applying the model to the investigation of RF blackout. Simulations are performed under thermochemical nonequilibrium conditions, specifically using a three-temperature model that accounts for translational-rotational, vibrational, and electron-electronic temperatures. In fig. 8, translational-rotational temperatures

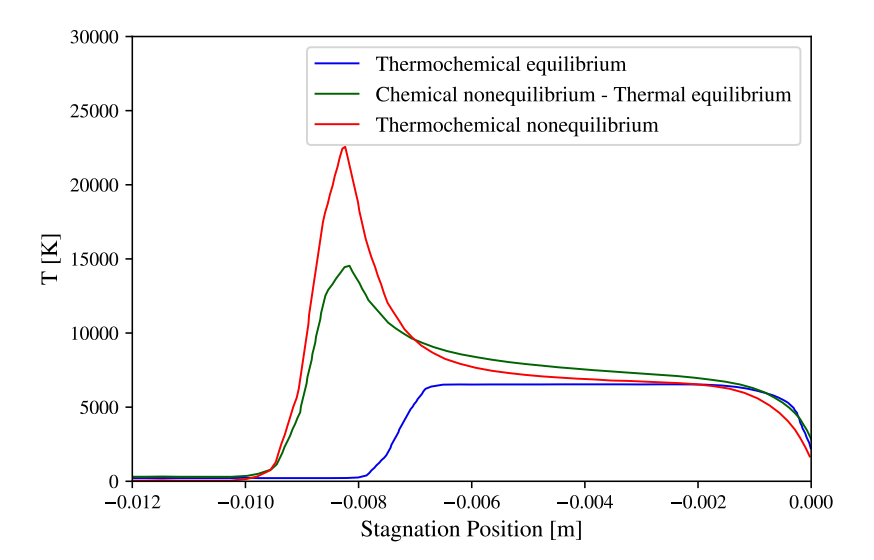


Fig 8. Comparaison of thermochemical equilibrium models on the stagnation line of the RAMC-II at 61 km.

atures along the stagnation line at 61 km altitude are shown for different thermochemical equilibrium models. The temperature varies approximately from 5,000 K under thermochemical equilibrium, to 15,000 K under chemical nonequilibrium, and up to 22,000 K when thermal nonequilibrium is considered. This significant difference highlights that thermal nonequilibrium should not be neglected under such reentry conditions. Indeed, it impacts directly the production of electrons. At high temperatures, chemical reactions, as ionization, are more likely to happen which produce ionized species. As presented in fig. 9, the studied flow is denser in electrons for a multi-temperatures simulation than for a mono-temperature one. Focusing on the distinction between the characteristic internal energy temperatures in fig. 10, the three different temperatures are computed along the stagnation line and compared to numerical results obtained by [7]. The three temperature profiles show significant differences from one another. Physically, the electrons are governed and influenced by electronic temperatures which is around 10,000K lower than the translational-rotational temperatures. Linked to the previous section on diffusion model, the effective coefficients should be applied for a thermal nonequilibrium model. To determine the effective diffusion coefficients, the Mutation++ library is used, computing them based on the local temperatures. In fig. 11, the multi-temperature model leads to a larger electron density compared to the single-temperature model. Moreover, when effective diffusion coefficients are applied, more electrons are produced than with the classical Lewis diffusion model.

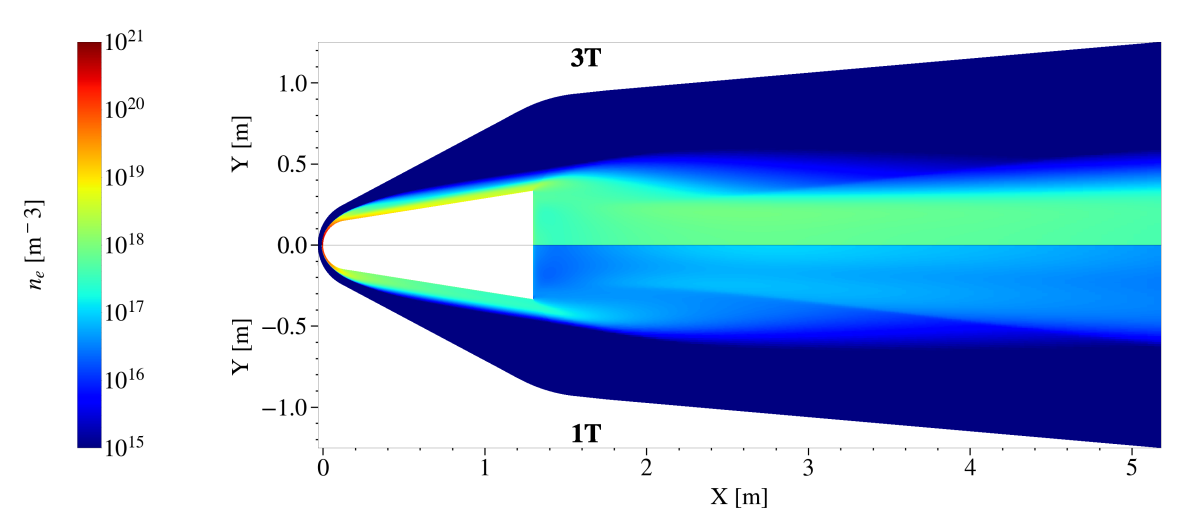


Fig 9. Comparaison of n_e in thermal nonequilibrium (top) and equilibrium (bottom) with Lewis diffusion coefficient at altitude 61km

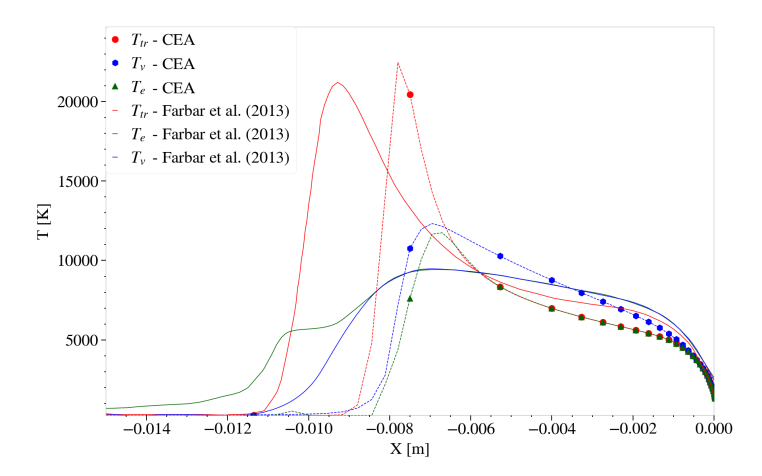


Fig 10. Comparaison of characteristic temperatures on the stagnation line of the RAMC-II at 61km in thermal nonequilibrium and Lewis diffusions with values obtaind by [4].

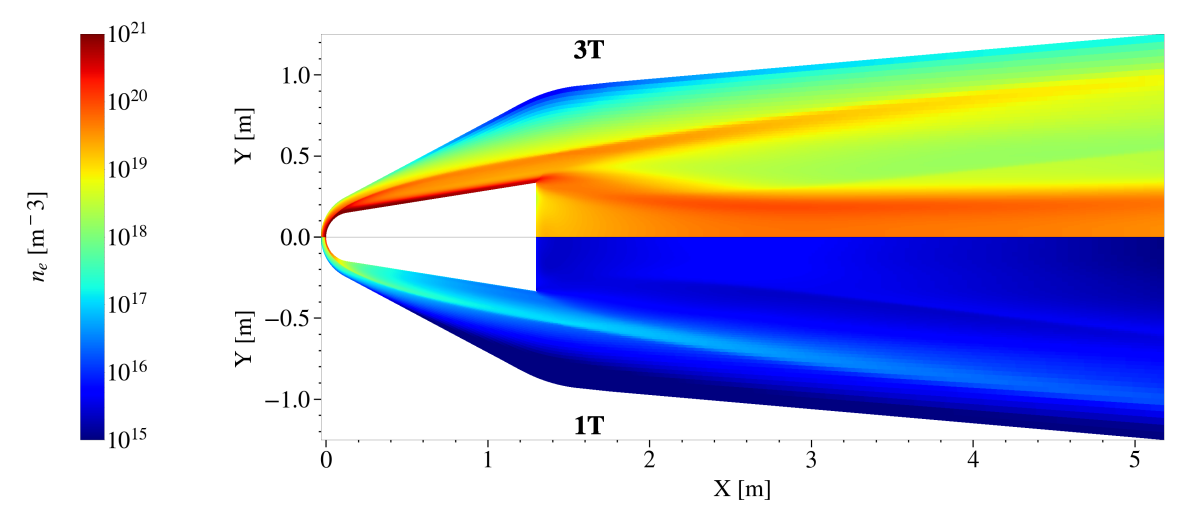


Fig 11. Comparaison of n_e in thermal nonequilibrium (top) and equilibrium (bottom) with effective diffusion coefficient at altitude 61km

However, up to now, these coefficients have been evaluated using only the translational temperature. This means that the effective diffusion coefficients are calculated solely using T_{tr} , while applying the thermal nonequilibrium equations presented (cf. eq. (6) and eq. (7)). If diffusion improvements are indeed linked to thermal nonequilibrium, then the effective diffusion coefficients for ionic species and electrons may differ and should ideally be computed using the electronic temperature as described in [17].

4.3. Signal Attenuation results

After the improvements outlined above, a comparison of signal attenuation is carried out for each modeling enhancement. The electric field value is calculated by determining the position of the frequency-specific antennas on the vehicle wall and the angle of incidence of the emitted signal from the corresponding satellite which are presented in [26]. In this section, two antennas are studied and presented in table 3. In general, communication waves at higher frequencies tend to be less attenuated in plasma, due

Anter	nna	Frequency [MHz]	Position on the wall [cm]	Blackout altitude [km]
VH	F	225.7	114.8	76 - 23
CBAI	ND	5800	106.7	51 - 38

Table 3. Information on studied antennas for the RAMC-II vehicle [1]

to their relationship with the critical electron density. From this perspective, VHF signals are expected to experience greater attenuation than C-band signals. After conducting the CEM simulations, the signal attenuation values are summarized in table 4. As expected, the CEM results confirm that the VHF

Altitude [km]	71	61	51
$G_{att,VHF}$ [dB]	0.6 - 1.4	1.0 - 11.9	5.0 - 13.5
$G_{att,CBAND}$ [dB]	0.0	0 - 0.1	0.0

Altitude [km]	61	51
$G_{att,VHF}$ [dB]	44.7 - 46.13	44.8 - 47.6
$G_{att,CBAND}$ [dB]	1.8 - 3.0	0.1 - 1.5

Table 4. Signal VHF (225, 7MHz) Signal Attenuation of the RAM C-II during reentry for effective diffusion (top) and multi-temperatures model with Lewis model (bottom)

signal experiences greater attenuation than the C-band signal at all altitudes. With the improved diffusion model, no RF blackout is predicted according to NASA's criterion (i.e., signal attenuation greater than $30\,\mathrm{dB}$). In contrast, RF blackout is observed when using the multi-temperatures model compared to mono-temperature model. However, on the top table, the attenuations are greater at an altitude of 51 km, consistent with experimental observations, in contrast to the Lewis model in mono-temperature (table 2), which predicts a peak at 61 km. Moreover, attenuations are greater when using the Lewis model. This means that the effective model is more accurate in predicting n_e at the wall, while the Lewis model performs better in calculating the global plasma layer under the mono-temperature assumption. Meanwhile, on the bottom table, the thermal nonequilibrium model tends to overestimate electron density along the wall, it provides a more accurate approximation within the plasma layer. As a result, signal attenuation is significantly increased throughout the different regions of the flow surrounding the vehicle, rather than being caused solely by the thin layer near the wall. For VHF frequencies, blackout is simulated at altitudes of 61 and 51 km. Additional simulations are needed to study attenuation below 51 km for the C-band. The current blackout prediction is inaccurate, and further work is ongoing to achieve this goal.

5. Conclusion

In this paper, the influence of aerodynamic phenomena on the behavior of the plasma layer surrounding a hypersonic reentry vehicle has been investigated. This study focuses on the influence of advanced diffusion models and thermal nonequilibrium effects on the prediction of electron density and signal attenuation during spacecraft reentry. The implementation of effective diffusion coefficients, calculated via the Mutation++ library, demonstrated significant improvements over classical Lewis diffusion, particularly in capturing the electron distribution upstream of the bow shock and extending the plasma sheath around the vehicle. Thermal nonequilibrium modeling, incorporating distinct translational-rotational, vibrational, and electronic temperatures, is shown to have a major impact in estimating electron density profiles, as it strongly affects plasma characteristics and signal attenuation.

Comparisons with experimental data from NASA's RAM-C II flights revealed that models using effective diffusion coefficients yield more reliable electron density predictions near the vehicle wall, while thermal nonequilibrium assumptions enhance accuracy within the plasma layer. Consequently, these improvements lead to a more realistic assessment of radio frequency (RF) blackout phenomena. The computational electromagnetics (CEM) simulations validated that signal attenuation is significantly influenced by these refined aerodynamic models, with VHF signals being more strongly attenuated than C-band signals across all studied altitudes.

Overall, this work underscores the critical role of precise thermochemical and transport modeling in understanding and predicting communication blackouts during atmospheric reentry. Future work should focus on further refining diffusion based on multi-components model [13], catalicity effects [21] and incorporating ablation effects [27] to enhance the fidelity of plasma layer characterization and RF blackout predictions. The study on the influence of electrophilic injection (RAMC-I and RAMC-III [1, 2]) is planned to assess the reliability of this solution in reducing RF blackout and to test the robustness of the in-house models implemented. Finally, it is necessary to run further computations based on data from other flight experiments (ARD, Stardust, etc.) and academic experiments to extend the range of conditions under which the models can be considered reliable.

References

- [1] Jones, W. L. J., and Cross, E. A., "Electrostatic-probe measurements of plasma parameters for two reentry flight experiments at 25 000 feet per second," 1972.
- [2] Weuver, W. L., and Bowen, J. T., "Entry trajectory, entry environment, and analysis of spacecraft motion for the RAM C-III flight experiment," 1972.
- [3] Isakeit, D., Watillon, P., Wilson, A., Cazaux, C., Bréard, G., and Leveugle, T., "The Atmospheric Reentry Demonstrator," 1998.
- [4] Farbar, E., Boyd, I. D., and Martin, A., "Numerical Prediction of Hypersonic Flowfields Including Effects of Electron Translational Nonequilibrium," *Journal of Thermophysics and Heat Transfer*, Vol. 27, No. 4, 2013, pp. 593–606. https://doi.org/10.2514/1.T3963.
- [5] Gorshkov, A. B., "Effect of physical and chemical nonequilibrium processes on the parameters of the near wake downstream of a spacecraft," *Fluid Dynamics*, Vol. 44, No. 5, 2009, p. 785–795. https://doi.org/10.1134/s0015462809050172.
- [6] Clarey, M. P., and Greendyke, R. B., "Thermochemical Nonequilibrium Processes in Weakly Ionized Air Using Three-Temperature Models," *Journal of Thermophysics and Heat Transfer*, Vol. 33, No. 2, 2019, pp. 425–440. https://doi.org/10.2514/1.T5536.
- [7] Kim, M., Gülhan, A., and Boyd, I. D., "Modeling of Electron Energy Phenomena in Hypersonic Flows," *Journal of Thermophysics and Heat Transfer*, Vol. 26, No. 2, 2012, pp. 244–257. https://doi.org/10.2514/1.T3716.
- [8] Surzhikov, S. T., "Numerical Simulation of Air Ionization in the RAM-C-II Flight Experiment," Fluid Dynamics, No. 2, 2022, pp. 279–298. https://doi.org/10.1134/s0015462822100639.

- [9] Takahashi, Y., Yamada, K., and Abe, T., "Prediction performance of blackout and plasma attenuation in atmospheric reentry demonstrator mission," *Journal of Spacecraft and Rockets*, Vol. 51, No. 6, 2014, p. 1954–1964. https://doi.org/10.2514/1.a32880.
- [10] Takahashi, Y., Yamada, K., and Takahashi, A., "Examination of Radio Frequency Blackout for Inflatable Vehicle During Atmospheric Reentry." *Journal of Spacecraft and Rockets*, Vol. 51, No. 2, 2014, pp. 430–441. https://doi.org/10.2515/1.A32539.
- [11] Wilke, C. R., "A Viscosity Equation for Gas Mixtures," The Journal of Chemical Physics, Vol. 18, No. 4, 1950, pp. 517–519. https://doi.org/10.1063/1.1747673.
- [12] Blottner, F. G., Johnson, M., and Ellis, M., "Chemically Reacting Viscous Flow Program For Multi-Component Gas Mixtures," 1971. https://doi.org/10.2172/4658539.
- [13] Sutton, K., and Gnoffo, P. A., "Multi-Component Diffusion with Application to Computational Aerothermodynamics," 7th AIAA/ASME Joint Thermophysics and Heat Transfer Conference, 1998. https://doi.org/10.2514/6.1998-2575.
- [14] Scoggins, J. B., Leroy, V., Bellas-Chatzigeorgis, G., Dias, B., and Magin, T. E., "Mutation++: MUlticomponent Thermodynamic And Transport properties for IONized gases in C++," SoftwareX, Vol. 12, 2020, p. 100575. https://doi.org/https://doi.org/10.1016/j.softx.2020.100575.
- [15] Ramshaw, J. D., and Chang, C. H., "Ambipolar Diffusion in Multicomponent Plasmas," *Plasma Chem Plasma Process*, No. 11, 1991, p. 395–402. https://doi.org/10.1007/BF01458919.
- [16] Desmeuzes, C., Duffa, G., and Dubroca, B., "Different levels of modeling for diffusion phenomena in neutral and ionized mixtures," *Journal of Thermophysics and Heat Transfer*, Vol. 11, No. 1, 1997, p. 36–44. https://doi.org/10.2514/2.6220.
- [17] Gnoffo, P., Gupta, R., and Shinn, J., Conservation Equations and Physical Models for Hypersonic Air Flows in Thermal and Chemical Nonequilibrium, NASA technical paper, National Aeronautics and Space Administration, Office of Management, Scientific and Technical Information Division, 1989.
- [18] Kundrapu, M., Loverich, J., Beckwith, K., Stoltz, P., Shashurin, A., and Keidar, M., "Modeling Radio Communication Blackout and Blackout Mitigation in Hypersonic Vehicles," *Journal of Spacecraft and Rockets*, Vol. 52, No. 3, 2015, p. 853–862. https://doi.org/10.2514/1.a33122.
- [19] Park, C., Jaffe, R. L., and Partridge, H., "A Review of Reaction Rates and Thermodynamic and Transport Properties for an 11-Species Air Model for Chemical and Thermal Nonequilibrium Calculations to 30 000 K," NASA TM-101528, 1990.
- [20] Stupfel, B., Le Martret, R., Bonnemason, P., and Scheurer, B., "Combined boundary-element and finite-element method for the scattering problem by axisymmetrical penetrable," Society for Industrial and Applied Mathematics (SIAM), Philadelphia, PA, 1991, p. 332–341.
- [21] Takahashi, Y., Enoki, N., Takasawa, H., and Oshima, N., "Surface catalysis effects on mitigation of radio frequency blackout in orbital reentry," *Journal of Physics D: Applied Physics*, Vol. 53, No. 23, 2020, p. 235203. https://doi.org/10.1088/1361-6463/ab79e0.
- [22] Hartunian, R., Stewart, G., Curtiss, T., Fergason, S., Seibold, R., and Shome, P., "Implications and mitigation of radio frequency blackout during reentry of Reusable Launch vehicles," AIAA Atmospheric Flight Mechanics Conference and Exhibit, 2007. https://doi.org/10.2514/6.2007-6633.
- [23] Park, C., "Review of chemical-kinetic problems of future NASA missions. I Earth entries," *Journal of Thermophysics and Heat Transfer*, Vol. 7, No. 3, 1993, pp. 385–398. https://doi.org/10.2514/3.431.
- [24] Park, C., "Assessment of Two-Temperature Kinetic Model for Ionizing Air," Journal of Thermophysics and Heat Transfer, Vol. 3, No. 3, 1989, pp. 233–244. https://doi.org/10.2514/3.28771.

- [25] Luís, D., Giangaspero, V., Viladegut, A., Lani, A., Camps, A., and Chazot, O., "Effect of electron number densities on the radio signal propagation in an inductively coupled plasma facility," Acta Astronautica, Vol. 212, 2023, pp. 408–423. https://doi.org/https://doi.org/10.1016/j.actaastro.2023. 07.028.
- [26] Takahashi, Y., "Advanced validation of CFD-FDTD combined method using highly applicable solver for reentry blackout prediction," Journal of Physics D: Applied Physics, Vol. 49, No. 1, 2015, p. 015201. https://doi.org/10.1088/0022-3727/49/1/015201.
- [27] Loridan, V., Peluchon, S., and Claudel, J., "Investigating the accuracy of a fully coupled fluid / thermal strategy with nonequilibrium chemistry to compute graphite ablation," AIAA AVIATION 2023 Forum, 2023. https://doi.org/10.2514/6.2023-3329.